

Therefore, the detection rate is $O(\sqrt{\eta})$. Strict security analysis shows that PM-QKD enjoys a quadratic improvement on the rate-transmittance performance over the original MDI-QKD[13].

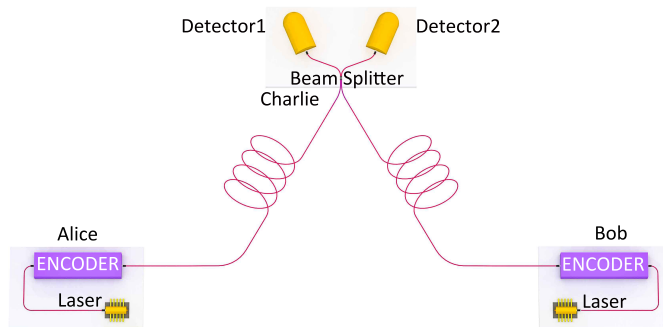


FIG. 1. **Schematic diagram of PM-QKD.** Encoder is a device to modulate the intensity μ and phase ϕ of coherent states. The beam splitter and the single photon detectors are used for interference detection. Divide the phases $\phi \in [0, 2\pi)$ into D slices, denoted by $\Delta_j = [\frac{\pi}{D}(2j-1), \frac{\pi}{D}(2j+1))$ with the index $0 \leq j \leq D-1$. In the experiment, we set $D = 16$. In each round of key distribution, Alice encodes a random bit κ_a into her coherent state $|\sqrt{\mu_a}e^{i(\kappa_a\pi+\phi_a)}\rangle$, after adding an extra discrete random phase $\phi_a = j_a 2\pi/D$ which is at the center of j_a th phase slice Δ_{j_a} . Similarly, Bob encodes κ_b , μ_b , and ϕ_b on his pulse, $|\sqrt{\mu_b}e^{i(\kappa_b\pi+\phi_b)}\rangle$. Alice and Bob then send their pulses to Charlie, who is supposed to interfere these quantum states to measure phase differences. After Charlie announces the detection results, Alice and Bob publicly announce the slice indexes j_a, j_b of the random phases. They post-select the key bits κ_a, κ_b as the raw key, according to Charlie's detection results and the sifting scheme depending on j_a, j_b , with the phase post-compensation technique.

Despite the promising qualities of PM-QKD on both security and performance, the experimental implementation is very challenging. In PM-QKD, the interference results at the measurement result should reflect the difference between Alice's and Bob's encoded phases. In practice, an essential requirement is to match the phases of coherent states generated by two remote and independent lasers. The coherent states of Alice $|\sqrt{\mu_a}e^{i(\kappa_a\pi+\phi_a)}\rangle$ and Bob $|\sqrt{\mu_b}e^{i(\kappa_b\pi+\phi_b)}\rangle$ could have different phase references due to phase drift and fluctuation. Define the reference deviation ϕ_δ to be the phase difference when both Alice and Bob set $\kappa_{a(b)} = 0$ and $\phi_{a(b)} = 0$. There are three main factors determining the value of ϕ_δ , fluctuations of the laser initial phases, fibre lengths, and laser frequencies. Take the 1550 nm telecom light through a 200 km fibre for example, either a tiny change of transmission time, say by 10^{-15} s corresponding to a 200 nm optical length, or a small deviation of the angular frequency, say by 1 kHz, will cause a significant phase drift. Note that, there are several recent experiments which make efforts to deal with these challenges in order to demonstrate the advantages of the new type of MDI-QKD schemes[15–18].

In this work, we implement PM-QKD with the setup shown in Fig. 2. In order to suppress the fluctuations of the laser initial phases and frequencies, we employ the laser injection technique[19]. The setups on Alice's and Bob's sides are exactly the same. Below, we take Alice's side for example. The master laser in between Alice and Bob, with 3 kHz line-width and 1550.12 nm centre wavelength, emits a seed light which goes through a long fibre to lock Alice's distributed feedback laser. Alice's laser generates optical pulses with a clock rate of 312.5 MHz. Two Sagnac rings are employed to modulate pulses into four different intensities. The pulses with the largest intensity are used as reference pulses for phase estimation, while the other three pulses are used as the signal state, weak decoy state, and vacuum state to implement the decoy-state method. The extinction ratio between the signal state and the vacuum state is about 20 dB. Two phase modulators are employed to modulate 16 different phases. Details of the laser injection technique and the phase estimation are presented in Appendix A and B.

The pulses from Alice and Bob are transmitted through long optical fibres and interfered at the measurement site. The interference results are detected by two superconducting nanowire single photon detectors. The dark count is about 10 counts per second and the detector efficiency is about 40%. The total detection efficiency reduces to about 23% owing to 1.2 dB insertion loss and 25% non-overlapping between signal and detection windows. Two stabilization systems are inserted before interference to filter out the noise caused by the nonlinear effect of the fibre and stabilizing the incident pulses. Details of the implementation are presented in Appendix D.

Due to fibre fluctuation, there exists a slow phase drift between Alice and Bob. In the case when the phase fluctuates slowly, pulses nearby share similar values of the reference deviation ϕ_δ . Inspired by this observation, we employ a simple phase post-compensation technique[20]. During the experiment, Alice and Bob send reference pulses and quantum pulses periodically. The reference pulse is typically more than one order of magnitude stronger than the quantum pulse. They use reference pulses to estimate which slice j_δ the reference deviation ϕ_δ lies in, according to interference results. They use quantum pulses to perform the PM-QKD experiment. After obtaining measurement results, Alice

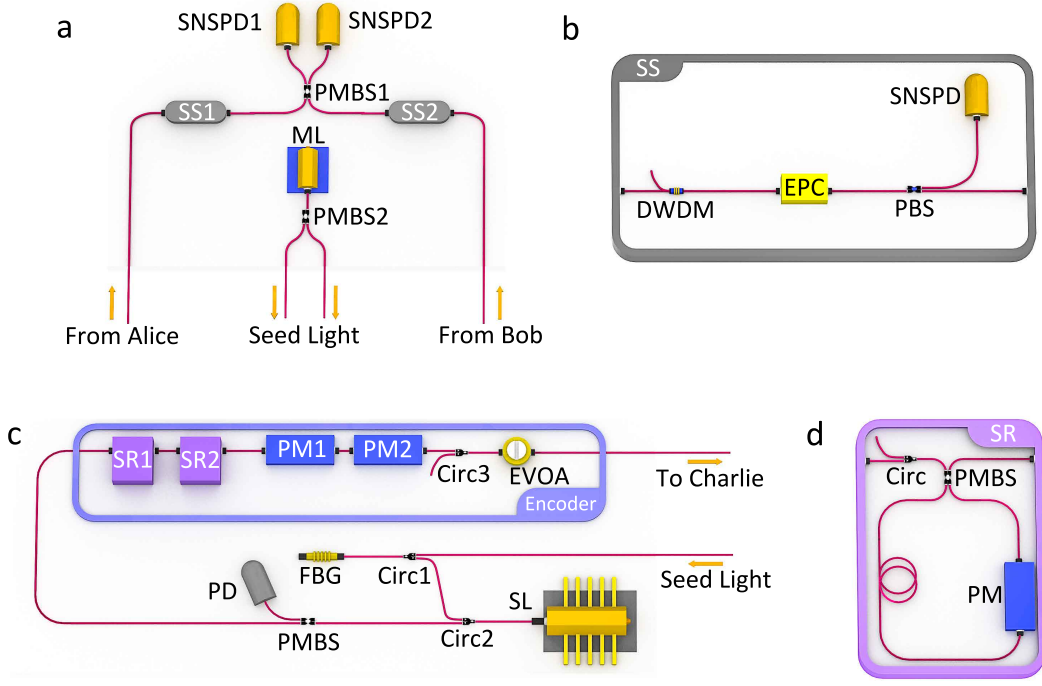


FIG. 2. **Experimental setup.** **a.** The continuous-wave master laser (ML), used as the phase and wavelength reference, are split by a polarization-maintaining beam splitter (PMBS2) and sent to Alice and Bob to lock their distributed feedback (DFB) lasers, which act as slave lasers (SLs). Two stabilization systems (SS1 and SS2) are placed to enhance the interference stability. Alice and Bob's pulses are interfered at PMBS1 and then detected by two superconducting nanowire single photon detectors (SNSPD1 and SNSPD2). **b.** Stabilization system. The dense wavelength division multiplexer (DWDM) filters out optical noises which disturb the detection results. A polarization beam splitter (PBS), an SNSPD, and an electric polarization controller (EPC) are used to ensure that the polarization of the two pulses from Alice and Bob are indistinguishable. **c.** Quantum source. Alice (same as Bob) injects the seed light from the ML, which is filtered by the fibre Bragg grating (FBG), into her local DFB laser as the slave laser (SL). The SL generates pulses, which are split by the PMBS. One of the output pulses goes to the encoder and the other is monitored by a photoelectric diode (PD). The encoder is composed of two Sagnac rings (SR1 and SR2) for modulating intensities and two phase modulators (PM1 and PM2) for encoding phases. A circulator (Circ3) is placed to isolate the source from the channel. The electrical variable optical attenuator (EVOA) reduces the pulse intensity down to the single-photon level. **d.** Sagnac ring. An SR includes a Circ, a PMBS, a PM, and optical fibre. The length difference between the optical fibre connected the output and input of the phase modulators are delicately designed to meet two times of the repetition frequency of the pulses.

and Bob publicly announce the random phase slices j_a, j_b of the signal pulses. They calculate $j_s = j_a - j_b + j_\delta$ for raw key sifting, where j_δ works as the post-compensation shift. Clearly, if j_δ accurately reflects the real-time reference deviation of the system, perfect interference will happen when $j_s = 0$ or $j_s = 8$. Note that the estimated phase slice indexes j_δ are only used in the post-processing, which frees us from active phase locking during the state transmission. Furthermore, compared with active locking, where the phase can only be locked well when ϕ_δ keeps stable during the whole process of phase estimation and feedback, the phase post-compensation method can tolerate faster fluctuation, as long as ϕ_δ does not change much in the time between the reference and quantum pulses.

In the security analysis of PM-QKD[13], due to the random phases Alice and Bob modulated on their coherent states, the joint state can be decomposed into odd and even total photon number components, ρ_{AB}^{odd} and ρ_{AB}^{even} . Denote the proportions of detection caused by ρ_{AB}^{odd} and ρ_{AB}^{even} as q^{odd} and q^{even} , respectively, and obviously, $q^{odd} + q^{even} = 1$. In fact, the information leakage in PM-QKD is shown to be independent of channel disturbance. As a result, the privacy is only related to q^{even} , irrelevant to the bit error rate. The final key length is given by

$$K = M_\mu [1 - H(q_\mu^{even})] - l_{cor}, \quad (1)$$

where $H(x) = -x \log_2 x - (1-x) \log_2 (1-x)$ is the binary entropy function. Here, we consider the case where Alice and Bob use the same intensities of coherent states. The subscript μ represents the signal states with $\mu_a = \mu_b = \mu/2$. The raw key length M_μ is the number of detection events caused by signal states when Alice and Bob match their phases, $j_s = 0$ or 8 . The even photon component ratio q_μ^{even} can be efficiently estimated by decoy state methods[3–5].

The error correction cost l_{cor} can be usually estimated by a function of bit error rate E_μ , $l_{cor} = fM_\mu H(E_\mu)$, where f is the error correction efficiency depending on $E_\mu^{j_s}$. The key rate is defined by $R = K/N$, where N is the number of QKD rounds. Details of the decoy state method and the security analysis by considering the finite data size effects are presented in Appendix E.

In order to further improve the key rate, one can take advantage of the data with mismatched phases. Note that the phase-mismatched signals of $j_s = 1, 9$ can be regarded as the ones with a fixed misalignment $\phi_\delta = 2\pi/D$, which results in a larger bit error rate compared with the phase-matched signals of $j_s = 0, 8$. The raw keys with different j_s have the same q^{even} in Eq. (1) and hence the same privacy. More explicitly, Alice and Bob can categorize the data from signal states into $D/2$ groups, where the data of $j_s = 0, 8$ are in the 0-th group, the data of $j_s = 1, 9$ are in the 1-st group, etc. Alice and Bob can correct errors in each data group separately and perform privacy amplification altogether. Of course, if the error rate in a group is too large, they can simply discard that group of data.

We perform the experiment via 101, 201, 302, 402 km standard optical fibres and a 502 km ultralow-loss optical fibre. The experiment parameters and results are presented in Fig. 3, from which one can see that the key rate-transmittance relation follows $R = O(\sqrt{\eta})$ as a contrast with the linear rate-transmittance bound. Specifically, the experimental results beat the linear bound at the distances of 302 and 402 km. Take the 302 km fibre case as an example, with the same channel transmission and detection efficiency, the linear key-rate bound is given by $R_{up} = 5.44 \times 10^{-7}$. Our experiment yields a key rate of $R = 6.74 \times 10^{-7}$, with a failure probability of $\epsilon = 1.68 \times 10^{-10}$, when all the mismatched data is used. The key rate is 24.0% higher than the bound. In the case of 302 km, the data with mismatched phases has a significant contribution to the overall key rate, which is 72.6% larger than the value with only the phase-matched group considered. Notably, our achieved key rate is three orders of magnitude higher than the asymptotic key rate of the original MDI-QKD scheme[6].

Meanwhile, we obtain a positive key rate at 502 km experiment with an ultralow-loss optical fibre, beating the current record of 421 km fibre communication distance of QKD[11]. The channel loss of 502 km experiment is 81.7 dB and the total loss is 87.1 dB. This new loss-tolerance record is comparable with the high-orbital satellite link loss in free space.

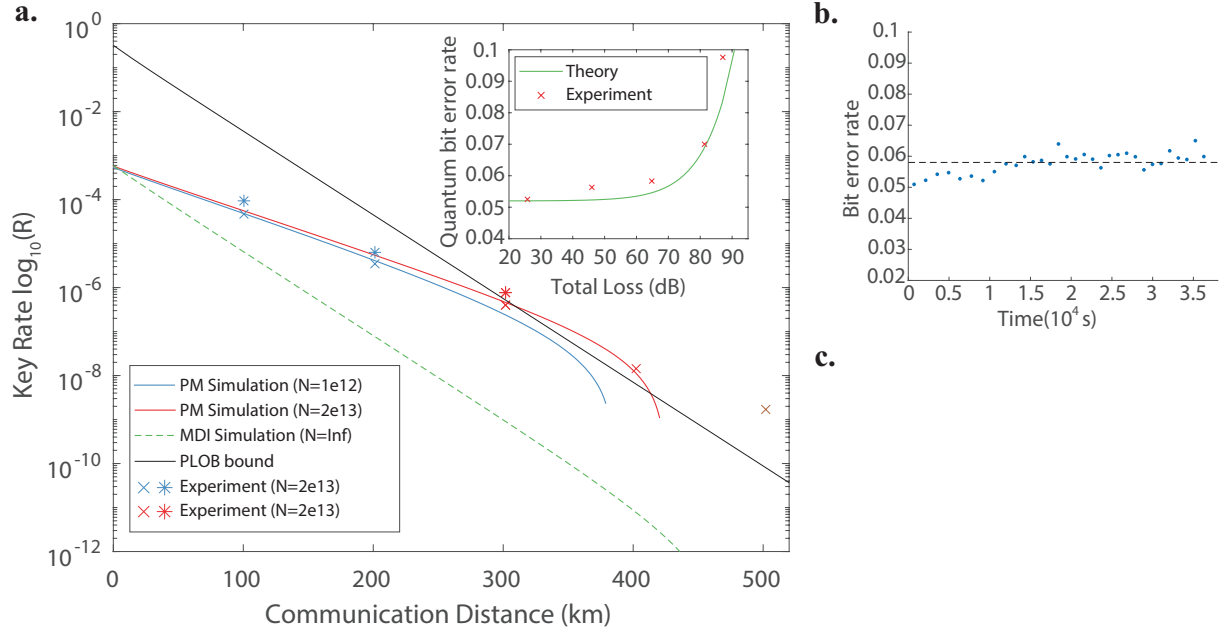


FIG. 3. **Experimental parameters and results.** **a.** Main panel, the experimental rate-distance performance of PM-QKD, comparing with the theoretical expectation and the linear key rate bound [9]. The data points marked by cross and star are, respectively, the key rate without and with the usage of phase-mismatched signals. Inset, error rate against total loss. The solid line shows the bit error rate in the theoretical model, and the crosses show the experiment data. **b.** The bit error rate with respect to the experiment time in the 302 km experiment. Each data point represents a number of 3.31×10^5 effective clicks which are collected in 21.91 minutes on average. The blue dots and red dots show the bit error rate for data with phase difference $j_d = 0$ and 1, respectively. **c.** Parameters used in the experiment and theoretical simulation. Note that, the listed value of the dark count rate p_d , the detection efficiency η_d , misalignment error e_d , and the fibre loss of PM-QKD are used for numerical simulation. The corresponding experimental values depend on the specific environment, which are listed in Appendix G.

Our results show that PM-QKD system is stable and economical, which facilitates the promotion of practical QKD. In the future, we expect to use the phase post-compensation technique to keep the system robust by increasing the system repetition frequency and enhancing the detectors' performance. Also, we expect that the design of PM-QKD experiment will be helpful for the construction of quantum repeater[21, 22], as well as extending the reach of the quantum internet.

FUNDING INFORMATION

This work has been supported by the National Key R&D Program of China (Grant No. 2017YFA0303903 and No. 2017YFA0304000), the Chinese Academy of Science, the National Fundamental Research Program, the National Natural Science Foundation of China (Grant No. 11875173, No. 61875182 and No. 11674193), Anhui Initiative in Quantum Information Technologies, and Fundamental Research Funds for the Central Universities (WK2340000083).

ACKNOWLEDGMENTS

We acknowledge H. Zhou for the insightful discussions.

AUTHOR CONTRIBUTIONS

All authors contributed extensively to the work presented in this paper.

AUTHOR INFORMATION

Reprints and permissions information is available at www.nature.com/reprints. The authors declare no competing financial interests. Readers are welcome to comment on the online version of this article at www.nature.com/nature.

Appendix A: Phase drift estimation

Rather than using extra devices to lock the phase, here we apply the phase estimation method to estimate the drifted phase, as shown in Fig. 4. Here, Alice and Bob need not obtain the exact value of the real-time phase deviation ϕ_δ , but only an estimation of the slice number j_δ for post-compensation. Moreover, the estimation of j_δ does not need to be announced in a real-time manner. Instead, it can be announced during the sifting process, as a post-selection shift factor. This makes our protocol practical without active feedback.

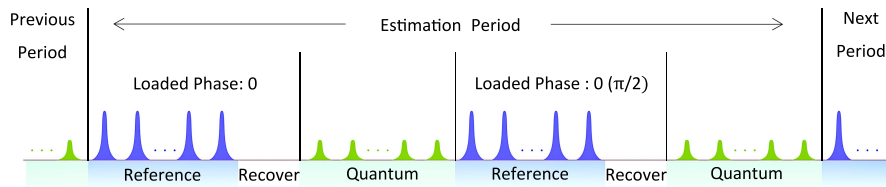


FIG. 4. **Phase estimation technique.** The pulses with a repetition rate of 312.5 MHz are grouped into trains, each containing 625 pulses. The period of pulse trains is about $2 \mu\text{s}$. In each train, there are two reference pulse regions and two quantum pulse regions. Alice loads the 0 and $\pi/2$ phase on her pulses in the former and latter reference pulse region, respectively. A recovery region without pulses is at the end of every reference pulse region, where the detector systems recover to the optimal working condition.

In the reference pulse region, Alice and Bob send reference pulses to Charlie, who interferes them and announces the results. They use the interference results to estimate the phase slice difference between two reference pulses, ϕ_δ .

The right detector click ratio P_r after interference is

$$\frac{n_r}{n_r + n_l} \approx P_r = \frac{1 + \cos \phi_\delta}{2}, \quad (\text{A1})$$

where n_r and n_l are the counts of the right and left detector clicks, respectively. With this ratio, one can classify the phase fluctuation ϕ_δ to the phase slices Δ_{j_δ} marked by j_δ according to the detection ratio.

Note that, since the phase deviation ϕ_δ and $(2\pi - \phi_\delta)$ yield the same P_r , Alice and Bob cannot discriminate these two cases from the ratio P_r . To solve this problem, Alice loads a $\phi_0 = \pi/2$ phase on the pulses in the latter reference pulse region, making the phase difference to be $\phi_\delta + \pi/2$, and hence $P_r = \frac{1 - \sin \phi_\delta}{2}$. In that case, one can distinguish the phase slice j_δ from $(16 - j_\delta)$. With the interference results P_r from the case $\phi_0 = 0$ and $\phi_0 = \pi/2$, Alice and Bob can estimate j_δ accurately, as shown in Fig. 5.

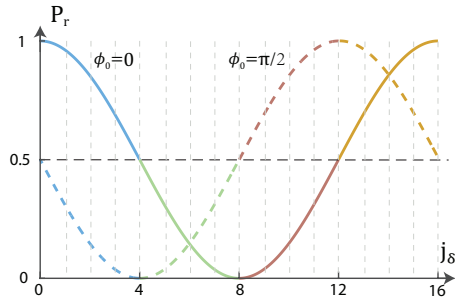


FIG. 5. **Phase estimation region.** The blue, green, red and orange region denotes four phase quadrants ranging from $[0, \pi/2)$, $[\pi/2, \pi)$, $[\pi, 3\pi/2)$, and $[3\pi/2, 2\pi)$. The solid line shows the theoretic detection probability P_r with the initial phase difference ϕ_0 of the reference pulse is set to 0, while the dashed line shows P_r when $\phi_0 = \pi/2$. From these two estimated P_r values, one can infer the j_δ value with no degeneracy.

In order to yield an accurate estimation of j_δ , sufficient detection counts of the reference pulses are required. According to the transmittance and phase drift velocity, one should properly set the intensity and time duration of the reference pulse and the system repetition frequency.

Appendix B: Laser injection technique

The fluctuation of reference deviation ϕ_δ is mainly caused by three factors: the initial phase fluctuation of the lasers, the optical length fluctuation, and the fluctuation of the laser frequencies. In order to minimize the fluctuation caused by the first and the third factors, we apply the laser injection technique.

As shown in Fig. 6a, a narrow line-width continuous wave laser at Charlie side works as the master laser, while DFB laser at Alice's (same as Bob's) side works as the slave laser. The seed light generated by the master laser is divided into two parts and sent to the two slave lasers through long fibres, which induces stimulated emission. In this case, the wavelength and phase of the light generated by the slave laser are the same as the seed light, which results in slower fluctuation of laser initial phases. For a local experiment test, interference results of pulses generated by slave lasers shows that the phase difference of two locked slave lasers fluctuates in a relatively low speed, which is presented in Fig. 6b. Here, the residual phase noise and fluctuation mainly come from the spontaneous emission in the slave lasers. Though the phase will fluctuate faster when the fibre gets longer, we can still get an effective phase estimation in this case.

In the 101, 201, 302 km experiments, the master laser is put at the middle point between Alice and Bob's laser. The fibres used to transmit seed light and the signal light are different but with the same length. Due to the limited power of the master laser and low transmittance value, in the 402 km and 502 km experiments, we place the master laser and the slave lasers locally.

Appendix C: PM-QKD protocol

In Box. C, we explicitly present the phase-matching quantum key distribution (PM-QKD) scheme implemented in the experiment. We divide the phase space $0 \sim 2\pi$ into D slices and denote the j -th slice as $\Delta_j = [\frac{\pi}{D}(2j-1), \frac{\pi}{D}(2j+1))$.

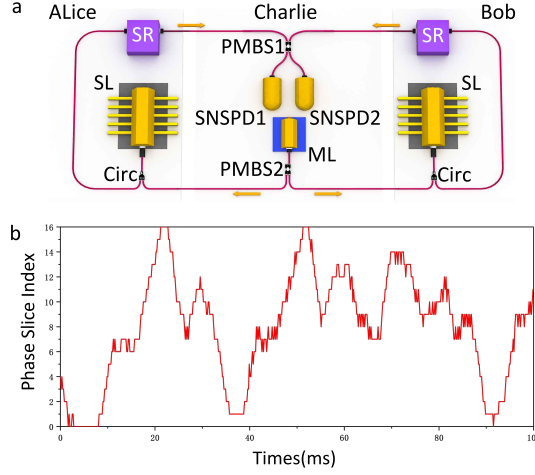


FIG. 6. **Laser injection technique and test.** **a.** Schematic implementation. **b.** Local drift test of the phase difference ϕ_δ with two local slave lasers. A statistic analysis on the detection data shows that the phase difference between the two locked slave lasers drifts at 0.62 rad/ms.

The central phase of j -th slice is $\phi_j = \frac{2\pi}{D}j$.

Suppose the phase references of Alice and Bob are different $\phi_a^{(0)}, \phi_b^{(0)}$. Moreover, we denote the phase variation in the fibre as ϕ_f . Before Eve's interference, the phase difference between Alice and Bob's pulses is

$$(\phi_a + \phi_a^{(0)}) - (\phi_b + \phi_b^{(0)}) + \phi_f = \phi_a - \phi_b + (\phi_a^{(0)} - \phi_b^{(0)} + \phi_f) = \phi_a - \phi_b + \phi_\delta \approx (j_a - j_b + j_\delta) \frac{2\pi}{D}, \quad (C1)$$

and hence the phase difference belongs to the $(j_a - j_b + j_\delta)$ -th slice. Suppose ϕ_δ fluctuates slowly with respect to time. By the interference of coherent pulses, Alice and Bob can estimate ϕ_δ accurately. In this case, for the data with $j_s = 0$, the interference should be nearly perfect, with small quantum bit error rate. Note that, the sifting strategy does not affect the security of PM-QKD. It only affects the error correction efficiency.

Appendix D: Experiment detail of PM-QKD

1. Laser injection details

As is shown in Fig. 7, the continuous wave emitted from the master laser (Realphoton Technology Ltd.) are split by a PMBS and transmitted through long fibres and finally injected into Alice and Bobs slave laser (Agilecom Ltd.). To achieve a good laser injection result, we apply the Erbium doped fiber amplifier (EDFA) to amplify the light intensity and the dense wavelength division multiplexer (DWDM) to filter the side band noise. After that, a fiber Bragg grating (FBG) inserted before injection is used to block the light with unexpected wavelength. A photoelectric diode (PD) is used to monitor the intensity of injection wave for avoiding that Charlie (or Eve) controls the output of the slave laser by manipulate the injection wave. The optical pulses at the width of 400 ps generated by the slave laser.

2. Encoding and measurement devices

In accordance with random bit values generated beforehand, two Sagnac rings [23] (SR1-2) are employed to modulate the intensities of reference state and three decoy states while two phase modulators (PM1-2) are employed to modulate encoding phases and random phases. The circulator followed are utilized to prevent Trojan horse attack. Note that the pulse into the SR is split into two pulses by the polarization-maintaining beam splitter (PMBS), one of which travels clockwise and the other travels anticlockwise. The PM in the SR adjusts and loads the phase only on one of the two pulses every round so that the output pulses intensity could be modulated when they meet again on the PMBS. To avoid the disturbance on the encoding process, the backward output pulses will be removed by the Circ

Box 1 | PM-QKD protocol

State preparation: Alice randomly generates a key bit κ_a , and picks a random phase ϕ_{j_a} from the set $\{j \frac{2\pi}{D}\}_{j=0}^{D-1}$, and the intensity μ_{i_a} from the set $\{0, \nu/2, \mu/2\}$. She then prepares the coherent state $|\sqrt{\mu_{i_a}} e^{i(\phi_{j_a} + \pi\kappa_a)}\rangle_A$. Similarly, Bob generates κ_b , ϕ_{j_b} , μ_{i_b} and then prepares $|\sqrt{\mu_{i_b}} e^{i(\phi_{j_b} + \pi\kappa_b)}\rangle_B$.

Measurement: Alice and Bob send their optical pulses, A and B , to an untrusted party, Eve, who is expected to perform an interference measurement and record the detector (L or R) that clicks.

Announcement: Eve announces her detection results. Then, Alice and Bob announce the random phases and intensities j_a, μ_{i_a} and j_b, μ_{i_b} , respectively.

Phase estimation: From time to time, Alice and Bob generate strong coherent pulses with $\phi_{j_a} = \phi_{j_b} = 0$ and send to Eve. Eve is supposed to interfere these pulses and estimate the phase difference ϕ_δ between these two pulses. Eve announces the phase slice number j_δ of ϕ_δ .

Alice and Bob repeat the above steps for N times. After that, they perform the following data post-processing procedures.

Sifting: When Eve announces a successful detection, (a click from exactly one of the detectors L or R), Alice and Bob keep κ_a and κ_b . Bob flips his key bit κ_b if Eve's announcement was an R click. Then, Alice and Bob group the signals by $j_s = (j_a - j_b + j_\delta) \bmod D$. If $j_s \in [\frac{D}{4}, \frac{3D}{4})$, Bob flips his key bit κ_b . After that, Alice and Bob merge the data with j_s and $j_s + \frac{D}{2}$, with $j_s = 0, 1, \dots, \frac{D}{2} - 1$.

Parameter estimation: For all the raw data that they have retained, Alice and Bob record the detect number $M_{i_a, i_b}^{(j_s)}$ of different intensity combinations $\{\mu_{i_a}, \mu_{i_b}\}$ and phase group j_s . They then estimate the phase error number among all the clicked signal rounds n_μ^X in the phase group j_s using the methods in Section E2.

Key distillation: For the signals with $\mu_{i_a} = \mu_{i_b} = \frac{\mu}{2}$, Alice and Bob group them by the phase difference j_s . They then perform error correction and error verification on the raw key data of each group j_s , respectively. They then perform privacy amplification on the sifted key bits to generate private key.

(circulator) in the SR. Because of the same fiber in which two pulses travel, the clockwise and counter-clockwise paths are insensitive to any length drifts or stress and temperature variation of the fiber within propagation time. In that case, the SR is so stable that the intensity feedback device is unnecessary.

In Charlie's measurement device, to make sure that the polarization of two pulses are indistinguishable, we utilize two PBSs before interfere to filter unexpected part. The reflection port of each PBS is monitored by the SNSPD with detection efficiency of 20% and dark count rate of 100 cps. Charlie adjusts the DC loaded in the EPC in real time to minimize and stabilize the detection count of SNSPD so the incident pulses intensity for interfere maintains maximum. Note that since we have to send strong reference pulses which is described in Appendix A, we always have enough pulses intensity for the polarization feedback system even the fiber length is up to 500 km, and Our feedback system works well with less than 1% loss of the incident pulse intensity.

The detector efficiency of SNSPD1 and SNSPD2 is about 40% in 101, 201, 302 and 402 km experiments, while in 502 km experiment, we enhance the efficiency of two detectors to 46% and 75% for better performance. To get a higher interference visibility, we set a 25% non-overlap between the signal and detection window. The insertion loss of Charlie's measurement device is about 1.2 dB.

3. Synchronization systems

The entire system are synchronized by two arbitrary-function generators (Tektronix, AFG3253) which is not shown in Fig. 1. Three 100 KHz electric signals in phase are modulated by two arbitrary-function generators. The delay between any two of them is adjustable. Alice, Bob and Charlie use one of them to regenerate their own 312.5 MHz system clock, respectively. To overlap the independent signal pulses from Alice and Bob precisely, we need to develop the time calibration system. First, Charlie measures the arriving time of the optical pulses from Alice and Bob with a time-to-digital converter (TDC), respectively. Then she adjusts the time delay between the electric signals from

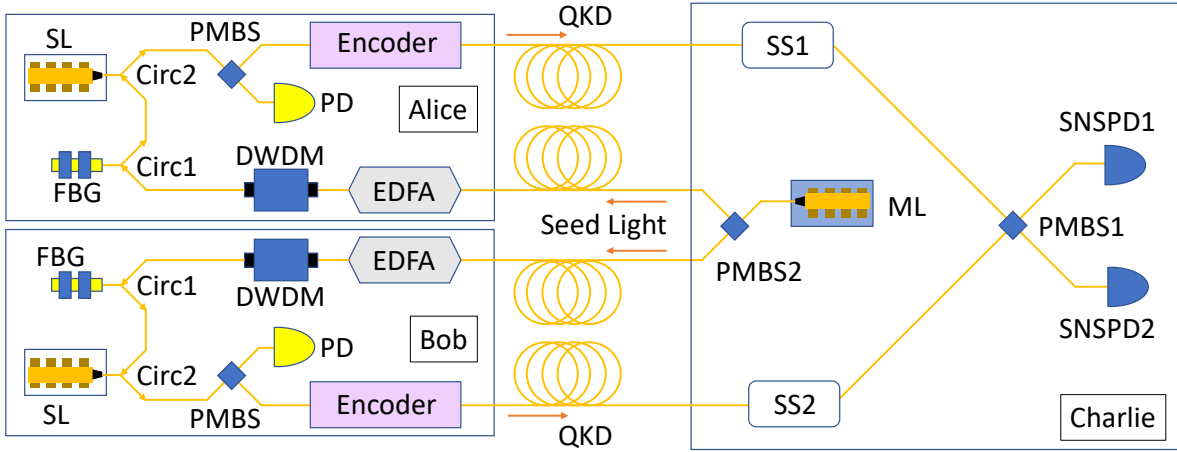


FIG. 7. Detailed setting of PM-QKD with the nonlocal laser locking system.

the arbitrary-function generator according to the calculation of the averaged arriving time. Due to the long optical fiber length drifting, we have to proceed a time calibration every 30 minutes. The total timing calibration precision is about 20 ps which is precise enough for the implement.

Appendix E: Finite-size parameter estimation

Here we list the formulas to estimate the key length K , the phase error number, and the corresponding failure probability. The detailed finite-size security analysis of PM-QKD is in Ref. [24].

1. Key length formula

In the experimental PM-QKD protocol introduced in Appendix C, Alice and Bob group the signals by the phase difference j_s . For the signals in group j_s , the key length is

$$K^{(j_s)} = M_\mu^{(j_s)} [1 - H(q_\mu^{even(j_s)})] - l_{cor}^{(j_s)}, \quad (E1)$$

where $M_\mu^{(j_s)}$ is the clicked rounds when Alice and Bob both send out signal lights with $\mu_{i_a} = \mu_{i_b} = \mu/2$ in the group j_s . $q_\mu^{even(j_s)}$ is the estimated fraction caused by the even state

$$q_\mu^{even(j_s)} = \frac{M_\mu^{even(j_s)}}{M_\mu^{(j_s)}}, \quad (E2)$$

where $M_\mu^{even(j_s)}$ is clicked rounds caused by even photon component in the $M_\mu^{(j_s)}$ with estimation method introduced in Appendix E 2.

The error correction cost, given by $l_{cor}^{(j_s)}$, can usually be estimated by a function of bit error rate $E_\mu^{(j_s)}$ among the signals of group j_s ,

$$l_{cor}^{(j_s)} = f M_\mu^{(j_s)} H(E_\mu^{(j_s)}), \quad (E3)$$

where f is the error correction efficiency, determined by the error rate $E_\mu^{(j_s)}$ and the specific error correction method. If $E_\mu^{(j_s)}$ is too large, the cost $l_{cor}^{(j_s)}$ may be larger than the generated key length $M_\mu^{(j_s)}(1 - H(q_\mu^{even(j_s)}))$. In this case, Alice and Bob directly abandon this group of data.

The overall key length for all the phase group j_s is

$$K = \sum_{j_s=0}^{D/2-1} \max_{j_s} \{K^{(j_s)}, 0\}. \quad (E4)$$

Note that, the information leakage is only related to the fraction $q_\mu^{even(j_s)}$, irrelevant to the bit error rate. Therefore, the overall information leakage depends on the even photon component in the clicked signals for all the phase group.

In practice, the data post-processing procedure can be improved. Alice and Bob can first perform error correction separately, with respect to different phase group j_s . If the error rate is too large, they can simply discard that group of data. Denote the group set J to be the set of group indices $\{j_s\}$ where the data is left. That is, if $j_s \in J$, then the phase group j_s is kept for key generation. For all the left phase groups in set J , Alice and Bob estimate the even photon fraction $q_\mu^{even(J)}$. They then perform privacy amplification among the left data altogether. Of course, Alice and Bob should properly set the group set J to maximize the key length.

With the improved post-processing procedure, the key length for the left phase groups is

$$K = M_\mu^{(J)}[1 - H(q_\mu^{even(J)})] - f \sum_{j_s \in J} M_\mu^{(j_s)} H(E_\mu^{(j_s)}), \quad (E5)$$

where $M_\mu^{(J)}$, $q_\mu^{even(J)}$ are, respectively, the clicked rounds and estimated even photon fractions for the left data.

2. Decoy-state estimation

The core of parameter estimation step is to estimate the phase error number $M_\mu^{even(J)}$ in the signal state group set J with $\mu_a = \mu_b = \mu/2$. According to the security analysis in Ref. [24], $M_\mu^{even(J)}$ is bounded by

$$M_\mu^{even(J)} = 1 - \sum_{k:odd} M_k^{s(J)} \geq 1 - M_1^{s(J)}, \quad (E6)$$

where $M_k^{s(J)}$ is the k -photon clicked number in the group set J of signal lights.

In experimental PM-QKD protocol, Alice and Bob set the signal, weak decoy and vacuum light with preset ratio r^s, r^w, r^{vac} . To estimate $M_1^{s(J)}$, Alice and Bob perform the following decoy-state process,

1. To record the sending round number when Alice and Bob both send out signal, weak decoy or vacuum pulses, denoted as $\{N^s, N^w, N^{vac}\}$; and the number of according single-clicked rounds (including the rounds with error), denoted as $\{M^s, M^w, M^{vac}\}$.
2. Based on an inversed usage of Chernoff bound introduced in Appendix E3, to calculate $\{\mathbb{E}^U(\bar{M}^a), \mathbb{E}^L(\bar{M}^a)\}_a$, where $a = s, w, vac$ as signal, weak decoy and vacuum pulse, and estimate the failure probability ϵ_1 . Calculate the $\{\mathbb{E}^U(\bar{Q}^a), \mathbb{E}^L(\bar{Q}^a)\}_a$ by

$$\bar{Q}^{a*} = \frac{\bar{M}^a}{N^a}. \quad (E7)$$

3. Calculate the minimal Y_1^{*L} based on $\{\mathbb{E}^U(\bar{Q}^{a*}), \mathbb{E}^L(\bar{Q}^{a*})\}_a$ and the following formula,

$$\bar{Y}_1^* \geq \bar{Y}_1^{*L} = \frac{\mu}{\mu\nu - \nu^2} \left(\mathbb{E}^L[\bar{Q}^{w*}]e^\nu - \mathbb{E}^U[\bar{Q}^{s*}]e^\mu \frac{\nu^2}{\mu^2} - \frac{\mu^2 - \nu^2}{\mu^2} \mathbb{E}^U[\bar{Q}^{vac*}] \right), \quad (E8)$$

calculate \bar{M}_k^L by

$$\bar{M}_k = N_k^\infty \bar{Y}_k^*, \quad (E9)$$

where

$$N_k^\infty = N \sum_a P^a(k) (r^a)^2, \quad (\text{E10})$$

are the asymptotic rounds of sending pulses with photon number k . $P^a(k)$ is the Poisson distribution when the intensity setting is a .

4. Based on a direct usage of Chernoff bound introduced in Appendix E 3, to calculate $(M_1^{s(J)})^L$ and estimate the failure probability ϵ_2 .

As a result, Alice and Bob can obtain an lower bound estimation of $M_1^{s(J)}$ with failure probability $\epsilon_1 + \epsilon_2$. From Eq. (E6), we can bound the phase error number $M_\mu^{\text{even}(J)}$.

3. Chernoff-Hoeffding bound

Here we present the methods to evaluate $\mathbb{E}(\bar{M}^a)$ from M^a and evaluate M_1^s from M_1 using Chernoff bounds.

To evaluate $\mathbb{E}(\bar{M}^a)$ from M^a , we inversely use the Chernoff bounds based on Bernoulli variables. We briefly summarize the results in Ref. [25]. For the observed value χ , we set the lower and upper bound of estimated $\mathbb{E}(\chi)$ as $\{\mathbb{E}^L(\chi), \mathbb{E}^U(\chi)\}$. Denote

$$\begin{aligned} \mathbb{E}^L(\chi) &= \frac{\chi}{1 + \delta^L}, \\ \mathbb{E}^U(\chi) &= \frac{\chi}{1 - \delta^U}. \end{aligned} \quad (\text{E11})$$

The failure probability of the estimation $\mathbb{E}(\chi) \in [\mathbb{E}^L(\chi), \mathbb{E}^U(\chi)]$, given by the Chernoff bound, is

$$\epsilon = e^{-\chi g_2(\delta^L)} + e^{-\chi g_2(\delta^U)}, \quad (\text{E12})$$

where $g_2(x) = \ln(1+x) - x/(1+x)$.

To evaluate M_1^s from M_1 , we directly apply the Chernoff bounds. Suppose the direct sampling expectation value of M_1^s is given by $\mathbb{E}(M_1^s) = p_1^s M_1$. For the expected value $\mathbb{E}(\chi)$, we set the lower and upper bound of the estimated χ as $\{\chi^L, \chi^U\}$. Denote

$$\begin{aligned} \chi^L &= (1 - \bar{\delta}^L) \mathbb{E}(\chi), \\ \chi^U &= (1 + \bar{\delta}^U) \mathbb{E}(\chi). \end{aligned} \quad (\text{E13})$$

The failure probability of the estimation $\chi \in [\chi^L, \chi^U]$, given by the Chernoff bound, is

$$\epsilon = e^{-(\bar{\delta}^L)^2 \mathbb{E}(\chi) / (2 + \bar{\delta}^L)} + e^{-(\bar{\delta}^U)^2 \mathbb{E}(\chi) / (2 + \bar{\delta}^U)}. \quad (\text{E14})$$

In practice, we can preset the lower bound and upper bound $\{\mathbb{E}^L(\chi), \mathbb{E}^U(\chi)\}$ or $\{\chi^L, \chi^U\}$ by assuming a Gaussian distribution on χ first,

$$\begin{aligned} \mathbb{E}^L(\chi) &= \chi - n_\alpha \sqrt{\chi}, & \mathbb{E}^U(\chi) &= \chi + n_\alpha \sqrt{\chi}, \\ \chi^L &= \chi - n_\alpha \sqrt{\mathbb{E}(\chi)}, & \chi^U &= \chi + n_\alpha \sqrt{\mathbb{E}(\chi)}, \end{aligned} \quad (\text{E15})$$

where n_α is a preset parameter to determine the estimation precision. After that, we calculate the failure probabilities by Eq. (E12) and Eq. (E14).

Appendix F: Simulation formulas and detailed results

Here we list the formulas used to simulate the key rate of PM-QKD and MDI-QKD in Fig. 3 in Main Text. The channel is modeled to be a pure loss one and symmetric for Alice and Bob with transmittance η (with the detector efficiency η_d) taken into account.

1. Gain, yield and error rate of PM-QKD

In PM-QKD, the k -photon the yield Y_k is (Eq. (B13) in Ref. [13])

$$Y_k \approx 1 - (1 - 2p_d)(1 - \eta)^k, \quad (\text{F1})$$

and the gain Q_μ when $\mu_a = \mu_b = \mu/2$, is (Eq. (B14) in Ref. [13])

$$Q_\mu \approx 1 - (1 - 2p_d)e^{-\eta\mu}. \quad (\text{F2})$$

The even signal fraction q_μ^{even} is bounded by

$$q_\mu^{even} \leq 1 - Y_1. \quad (\text{F3})$$

For the coherent lights with intensities $\mu_a - \mu_b = \mu/2$ and phase difference $\phi_a - \phi_b = \phi_\delta$, the bit error rate is (Eq. (B21) in Ref. [13])

$$E_\mu^Z(\phi_\delta) \approx \frac{e^{-\eta\mu}}{Q_\mu} [p_d + \eta\mu \sin^2(\frac{\phi_\delta}{2})]. \quad (\text{F4})$$

In the simulation in Fig. 3 in Main Text, we directly set $e_d(0) = 5.3\%$ and only consider the data with matched phases. The bit error rate is,

$$E_\mu^Z(0) \approx [p_d + \eta\mu e_d(0)] \frac{e^{-\eta\mu}}{Q_\mu}. \quad (\text{F5})$$

2. Simulation formulas for MDI-QKD protocols

The key rate of MDI-QKD is [6]

$$R_{MDI} = \frac{1}{2} \{ Q_{11} [1 - H(e_{11})] - f Q_{rect} H(E_{rect}) \}, \quad (\text{F6})$$

where $Q_{11} = \mu_a \mu_b e^{-\mu_a - \mu_b} Y_{11}$ and $1/2$ is the basis sifting factor. We take this formula from Eq. (B27) in Ref. [20]. In simulation, the gain and error rates are given by

$$\begin{aligned} Y_{11} &= (1 - p_d)^2 \left[\frac{\eta_a \eta_b}{2} + (2\eta_a + 2\eta_b - 3\eta_a \eta_b) p_d + 4(1 - \eta_a)(1 - \eta_b) p_d^2 \right], \\ e_{11} &= e_0 Y_{11} - (e_0 - e_d) (1 - p_d^2) \frac{\eta_a \eta_b}{2}, \\ Q_{rect} &= Q_{rect}^{(C)} + Q_{rect}^{(E)}, \\ Q_{rect}^{(C)} &= 2(1 - p_d)^2 e^{-\mu'/2} [1 - (1 - p_d) e^{-\eta_a \mu_a / 2}] [1 - (1 - p_d) e^{-\eta_b \mu_b / 2}], \\ Q_{rect}^{(E)} &= 2p_d (1 - p_d)^2 e^{-\mu'/2} [I_0(2x) - (1 - p_d) e^{-\mu'/2}]; \\ E_{rect} Q_{rect} &= e_d Q_{rect}^{(C)} + (1 - e_d) Q_{rect}^{(E)}, \end{aligned} \quad (\text{F7})$$

Here,

$$\begin{aligned} \mu' &= \eta_a \mu_a + \eta_b \mu_b, \\ x &= \frac{1}{2} \sqrt{\eta_a \mu_a \eta_b \mu_b}, \end{aligned} \quad (\text{F8})$$

where μ' denotes the average number of photons reaching Eve's beam splitter, and $\mu_a = \mu_b = \mu/2$, $\eta_a = \eta_b = \eta$. We take these formulas from Eqs. (A9), (A11), (B7), and (B28)-(B31) in Ref. [20].

In 2014, Takeoka *et al.* derived an upper bound of the key rate of the point-to-point-type QKD protocols [8],

$$R_{TGW} = -\log_2\left(\frac{1-\eta}{1+\eta}\right). \quad (\text{F9})$$

Later, Pirandola *et al.* established a tight upper bound [9],

$$R_{PLOB} = -\log_2(1-\eta), \quad (\text{F10})$$

which is the linear key-rate bound used in Main Text.

Appendix G: Experimental data

Here we list the experiment data for reference. Table I and II illustrate the data for theoretical parameters, channel condition and the key length calculation. Table III show the sending and received statistics of all the signals. Table IV and Table V shows the detailed data of 101 km experiment with different phase slices setting.

TABLE I. Parameter setting

Error correction efficiency	1.1
Failure probability	$\sim 1.7 \times 10^{-10}$
Fluctuation factor	7

TABLE II. Channel condition and key generation

Distance (km)	101	201	302	402	502
Channel loss	1.02E-1	1.05E-2	1.29E-3	1.91E-4	8.18E-5
detection loss	23%	23%	23%	20%	29%
Total loss(double side)	2.40E-03	2.53E-05	3.77E-07	7.34E-09	1.96E-09
Dark count	2.29E-07	5.85E-08	7.75E-08	3.36E-08	1.26E-08
PLOB bound	3.47E-03	3.66E-05	5.44E-07	1.06E-08	2.82E-09
intensity of decoy state(single side)	0.0179	0.0182	0.0192	0.0177	0.0127
intensity of signal state(single side)	0.0358	0.0364	0.0384	0.0353	0.0253
Sending rounds	1010250633000	1001472066000	20000133132000	19996635312500	20003396875000
Aligned bit error rate	5.31%	5.75%	6.06%	7.00%	9.80%
Key length	98957100	6502240	13479300	287710	33674
Aligned key length	48529900	3440190	7809030	287710	33674
Expansion factor	2.04	1.89	1.73	1.00	1.00
Failure probability	1.68E-10	1.67E-10	1.68E-10	1.69E-10	1.71E-10
Key Rate(bps)	2.06E+04	1.36E+03	9.44E+01	2.01E+00	1.18E-01

-
- [1] C. H. Bennett and G. Brassard, in Proceedings of the IEEE International Conference on Computers, Systems and Signal Processing (IEEE Press, New York, 1984) pp. 175–179.
- [2] A. K. Ekert, Phys. Rev. Lett. **67**, 661 (1991).
- [3] W.-Y. Hwang, Phys. Rev. Lett. **91**, 057901 (2003).
- [4] H.-K. Lo, X. Ma, and K. Chen, Phys. Rev. Lett. **94**, 230504 (2005).
- [5] X.-B. Wang, Phys. Rev. Lett. **94**, 230503 (2005).
- [6] H.-K. Lo, M. Curty, and B. Qi, Phys. Rev. Lett. **108**, 130503 (2012).

TABLE III. Experimental data of all signals

Distance (km)		101	201	302	402	502
Sending rounds	Vacuum state	48107173	453046887	25000166415	147832268203	414356078125
	Decoy state	6975540085	23129235810	280716154317	1352629545781	3020512928125
	Signal state	836776167162	684363089673	14331523970016	8554989086016	4369313403125
Received rounds (without alignment)	Vacuum state	22	53	3875	9931	10413
	Decoy state	6036008	2052221	3177133	1930178	1912753
	Signal state	1365570236	120111317	325475042	23839645	5367776
Received rounds of $j_d = 0$	Vacuum state	2	10	430	1273	1378
	Decoy state	764808	254969	397127	240748	238877
	Signal state	170644117	15018534	40698151	2982369	669910
Erroneous rounds of $j_d = 0$	Vacuum state	1	5	215	623	689
	Decoy state	45972	15921	28982	18418	35874
	Signal state	9063823	863533	2467769	208910	65623
Received rounds of $j_d = 1$	Vacuum state	2	10	502	1177	1240
	Decoy state	754770	257611	398227	241664	239632
	Signal state	170615800	15014075	40701711	2981797	671469
Erroneous rounds of $j_d = 1$	Vacuum state	1	5	251	583	620
	Decoy state	62393	17727	34677	28346	34094
	Signal state	12678651	1098100	2997090	287194	105489

- [7] Y.-L. Tang, H.-L. Yin, S.-J. Chen, Y. Liu, W.-J. Zhang, X. Jiang, L. Zhang, J. Wang, L.-X. You, J.-Y. Guan, *et al.*, *IEEE Journal of Selected Topics in Quantum Electronics* **21**, 116 (2014).
- [8] M. Takeoka, S. Guha, and M. M. Wilde, *Nat. Commun.* **5**, 5235 (2014).
- [9] S. Pirandola, R. Laurenza, C. Ottaviani, and L. Banchi, *Nat. Commun.* **8**, 15043 (2017).
- [10] H.-L. Yin, T.-Y. Chen, Z.-W. Yu, H. Liu, L.-X. You, Y.-H. Zhou, S.-J. Chen, Y. Mao, M.-Q. Huang, W.-J. Zhang, H. Chen, M. J. Li, D. Nolan, F. Zhou, X. Jiang, Z. Wang, Q. Zhang, X.-B. Wang, and J.-W. Pan, *Phys. Rev. Lett.* **117**, 190501 (2016).
- [11] A. Boaron, G. Boso, D. Rusca, C. Vulliez, C. Autebert, M. Caloz, M. Perrenoud, G. Gras, F. Bussi eres, M.-J. Li, D. Nolan, A. Martin, and H. Zbinden, *Phys. Rev. Lett.* **121**, 190502 (2018).
- [12] M. Lucamarini, Z. Yuan, J. Dynes, and A. Shields, *Nature* **557**, 400 (2018).
- [13] X. Ma, P. Zeng, and H. Zhou, *Phys. Rev. X* **8**, 031043 (2018).
- [14] J. Lin and N. L utkenhaus, *Phys. Rev. A* **98**, 042332 (2018).
- [15] M. Minder, M. Pittaluga, G. Roberts, M. Lucamarini, J. Dynes, Z. Yuan, and A. Shields, *Nature Photonics*, 1 (2019).
- [16] Y. Liu, Z.-W. Yu, W. Zhang, J.-Y. Guan, J.-P. Chen, C. Zhang, X.-L. Hu, H. Li, T.-Y. Chen, L. You, *et al.*, arXiv preprint arXiv:1902.06268 (2019).
- [17] S. Wang, D.-Y. He, Z.-Q. Yin, F.-Y. Lu, C.-H. Cui, W. Chen, Z. Zhou, G.-C. Guo, and Z.-F. Han, *Phys. Rev. X* **9**, 021046 (2019).
- [18] X. Zhong, J. Hu, M. Curty, L. Qian, and H.-K. Lo, arXiv preprint arXiv:1902.10209 (2019).
- [19] M. Lipka, M. Parniak, and W. Wasilewski, *Applied Physics B* **123**, 238 (2017).
- [20] X. Ma and M. Razavi, *Phys. Rev. A* **86**, 062319 (2012).
- [21] M. Zukowski, A. Zeilinger, M. A. Horne, and A. K. Ekert, *Phys. Rev. Lett.* **71**, 4287 (1993).
- [22] H.-J. Briegel, W. D ur, J. I. Cirac, and P. Zoller, *Phys. Rev. Lett.* **81**, 5932 (1998).
- [23] R. A. Bergh, in *Fiber optic and laser sensors X*, Vol. 1795 (International Society for Optics and Photonics, 1993) pp. 126–135.
- [24] P. Zeng, W. Wu, and X. Ma, Under preparation.
- [25] Z. Zhang, Q. Zhao, M. Razavi, and X. Ma, *Phys. Rev. A* **95**, 012333 (2017).

TABLE IV. Detailed data I of 101 km

Phase Slice	OPD 0		OPD 1		OPD 2		OPD 3		OPD 4		OPD 5		OPD 6		OPD 7	
	DETL	DETR	DETL	DETR	DETL	DETR	DETL	DETR	DETL	DETR	DETL	DETR	DETL	DETR	DETL	DETR
0	375744	3969399	185800	4164734	271002	4063293	615330	3766020	1196397	3213057	1844228	2403935	2539314	1633970	3081410	933133
1	537284	6098291	322140	6338669	513007	6265998	1125056	5733702	1979511	4666717	3035333	3521159	3986194	2309012	4963645	1354001
2	435376	4551069	232993	4891727	365819	4882103	791599	4348193	1468795	3648462	2223757	2723039	3093557	1878854	3745004	1062031
3	414272	4708067	235091	5042261	381802	4818464	839365	4361518	1484969	3562085	2337189	2748193	3107710	1806382	3874772	1042503
4	430329	5080877	259194	5201990	443091	5065594	911594	4466863	1673594	3780426	2497162	2796171	3416097	1894911	4085431	1034986
5	422237	4868334	276350	5083603	451102	4817269	968904	4409499	1672502	3595558	2565630	2742120	3372691	1768244	4170166	1027539
6	421145	4748597	275524	4828410	479551	4753741	958365	4199669	1703840	3526144	2521076	2564003	3413853	1752309	4019548	929900
7	469004	5140467	320768	5437178	511651	5188944	1066672	4744950	1848169	3811145	2825253	2954097	3681213	1868314	4541764	1058875
8	675823	5205534	362861	5409495	497550	5391926	1025723	4774534	1906743	4130350	2908171	3028818	4056797	2089810	4947662	1177153
9	751984	6139958	434122	6569900	556244	6260261	1136504	5862130	2024360	4742649	3189714	3687752	4316086	2449242	5343228	1436882
10	643626	4677926	298356	4877353	318169	4994816	666614	4464679	1323498	3880965	2147292	2959587	3041639	2066012	3858366	1214171
11	621568	4660951	301434	5115293	304863	4937140	673244	4647285	1326509	3885424	2167386	3036619	3074137	2076242	3878727	1234517
12	613155	4773223	270746	4953358	299752	5010456	667994	4535278	1311570	3871742	2144461	2969043	3014039	2044082	3890471	1227363
13	503642	4341689	236014	4707312	283689	4579890	634603	4215814	1252688	3537445	2010096	2713404	2875329	1890374	3711009	1116104
14	494467	4453118	239784	4642063	306664	4583053	683584	4154620	1300011	3478188	2112338	2713138	3011225	1869033	3679400	1075603
15	570313	5111750	287062	5418330	373937	5281927	817979	4793549	1578897	4101838	2573643	3187046	3485923	2131474	4361228	1252783

TABLE V. Detailed data II of 101 km

Phase Slice	OPD 8		OPD 9		OPD 10		OPD 11		OPD 12		OPD 13		OPD 14		OPD 15	
	DETL	DETR	DETL	DETR	DETL	DETR	DETL	DETR	DETL	DETR	DETL	DETR	DETL	DETR	DETL	DETR
0	3576331	462675	3698372	227367	3688156	309506	3282896	668922	2818592	1292424	2062095	2012194	1419362	2827226	792026	3473682
1	5472601	638783	5808385	372595	5511681	554043	5077090	1193416	4055062	2127494	3099272	3322797	2013053	4443404	1148543	5447888
2	4311221	508294	4439892	248592	4426118	355970	3870006	784039	3288139	1504538	2438585	2351494	1647443	3244658	925502	4016093
3	4281037	469627	4571805	247678	4291668	359623	3937971	823162	3203771	1539792	2421228	2412460	1588343	3304423	886645	4069628
4	4676434	499303	4710458	249121	4648901	397609	4089283	893256	3391403	1660164	2506369	2583865	1638318	3507512	924505	4404040
5	4526437	447099	4780554	244226	4534353	403877	4067129	894940	3314316	1652777	2439324	2547910	1621141	3530837	904895	4423635
6	4560390	432379	4646425	241914	4481594	403693	3960067	897943	3209832	1635793	2415660	2565777	1591514	3547321	867169	4225159
7	4984117	477533	5172315	272093	4938549	452297	4357280	995027	3625455	1847187	2724208	2901542	1749707	3833764	983822	4681210
8	5634057	564788	5895012	287022	5712734	410723	5275605	912910	4492060	1761009	3354542	2699309	2285034	3710025	1318072	4493231
9	6055441	695599	6325427	393846	6308054	549074	5848996	1179938	4813596	2108247	3704310	3276566	2495890	4357721	1520550	5486773
10	4442634	600914	4864009	287216	4957478	335079	4497613	724541	3864613	1415560	2969901	2223641	2124926	3193987	1254639	3980210
11	4590026	612811	5036806	289969	4908022	334996	4556779	744118	3828204	1403545	3050678	2321539	2081010	3222761	1279160	4130325
12	4612559	601061	4835746	288726	4818202	348755	4360038	734421	3795422	1446993	2895683	2295465	2048632	3271887	1198245	4027685
13	4181277	535961	4470633	271225	4335119	325771	4059576	728951	3374100	1362937	2660620	2210587	1792712	3014752	1091187	3880884
14	4221721	530266	4381533	271406	4394063	364214	3946303	752179	3398431	1428086	2558102	2213075	1800125	3134338	1009909	3820870
15	4876569	606080	5261246	332588	5087582	415528	4737267	890003	3913291	1638705	3090211	2641099	2023280	3578779	1204437	4537282